Ultrasoft microwire neural electrodes improve chronic tissue integration

Zhanhong Jeff Du[a,b,c,f,1], **Christi L. Kolarcik**[a,b,c,d,1], **Takashi D.Y. Kozai**[a,b,c,e], **Silvia D. Luebben**[g], **Shawn A. Sapp**[h], **Xin Sally Zheng**[a], **James A. Nabity**[i], and **X. Tracy Cui**[a,b,c,*]

[a]Department of Bioengineering, University of Pittsburgh, PA, USA

[b]Center for the Neural Basis of Cognition, University of Pittsburgh, PA, USA

[c]McGowan Institute for Regenerative Medicine, University of Pittsburgh, PA, USA

[d]Systems Neuroscience Institute, University of Pittsburgh, PA, USA

[e]NeuroTech Center of Brain Institute, University of Pittsburgh, PA, USA

[f]Shenzhen Key Lab of Neuropsychiatric Modulation, CAS Center for Excellence in Brain Science, Shenzhen Institutes of Advanced Technology, Chinese Academy of Sciences, Shenzhen, China

[g]Boulder Scientific Company, Longmont, CO,USA

[h]Aei Corporation, Littleton, CO,USA

[i]Department of Aerospace Engineering Sciences, University of Colorado, Boulder, CO,USA

Abstract

Chronically implanted neural multi-electrode arrays (MEA) are an essential technology for recording electrical signals from neurons and/or modulating neural activity through stimulation. However, current MEAs, regardless of the type, elicit an inflammatory response that ultimately leads to device failure. Traditionally, rigid materials like tungsten and silicon have been employed to interface with the relatively soft neural tissue. The large stiffness mismatch is thought to exacerbate the inflammatory response. In order to minimize the disparity between the device and the brain, we fabricated novel ultrasoft electrodes consisting of elastomers and conducting polymers with mechanical properties much more similar to those of brain tissue than previous neural implants. In this study, these ultrasoft microelectrodes were inserted and released using a stainless steel shuttle with polyethyleneglycol (PEG) glue. The implanted microwires showed functionality in acute neural stimulation. When implanted for 1 or 8 weeks, the novel soft implants demonstrated significantly reduced inflammatory tissue response at week 8 compared to tungsten wires of similar dimension and surface chemistry. Furthermore, a higher degree of cell body distortion was found next to the tungsten implants compared to the polymer implants. Our results support the use of these novel ultrasoft electrodes for long term neural implants.

[*]Corresponding author at: Department of Bioengineering, University of Pittsburgh, 5057 Biomedical Science Tower 3, 3501 Fifth Avenue, Pittsburgh, PA 15260, USA., xic11@pitt.edu (X.T. Cui).
[1]These authors contributed equally to this work.

1. Introduction

Implantable neural electrodes or multielectrode arrays (MEAs) can record neuronal activity from individual or small populations of neurons [1]. Neural signals recorded by implantable MEAs provide valuable information for systems neuroscience research, enabling researchers to gain insight into functional neural networks used in sensory processing [2], motor control [3] and cognitive functions [4]. Neural signals recorded can also be utilized clinically to control brain-computer interfaces (BCI) for the restoration of lost neural functions [5–12] or to understand the basis of neurological dysfunction [13,14]. Alternatively, electrical signals can be delivered by MEAs to modulate neural network activity, in order to substitute lost sensory input [15] or to treat the symptoms of a neural disease. In recent years, such neural stimulation treatments have expanded to include not only motor dysfunction in Parkinson's disease [16] and neural network hyperactivity in epilepsy [17] but mental disorders such as depression [18] and obsessive compulsive disorder (OCD) [19].

One of the major challenges limiting the widespread use of neural implants in clinical applications is that these chronic devices fail over time. In the monkey cortex, previous reports indicated a 40% drop in the number of functional electrodes within 30 days [20]. The recorded action potential amplitude was also reported to decrease at the rate of 2.4% per month [21], which detrimentally impacts the outputs of decoding algorithms used in BCI [1]. Similar device performance degradation is observed in rodent studies [22–27]. Likewise, current clinical deep brain stimulation (DBS) implants could benefit tremendously from improved electrode technology. The DBS electrode surface impedance increases rapidly following implantation due to scar tissue encapsulation [28–30]. This decreases the effective range of the DBS electrode, increases battery drainage and causes variation in therapeutic effects [31]. Conventional DBS electrodes display large trial-to-trial variation which cannot be explained by known mechanisms [32]. Despite the decrease of impedance following neural stimulation [30,33], possibly caused by the disruption of tissue encapsulation, the heightened and varying electrode impedance could be the cause of these unpredictable and variable neural stimulation effects.

One proposed primary mechanism of such device failure is the foreign body response of the brain [34,35]. MEA implantation damages the blood brain barrier (BBB) and exposes a portion of the brain to substances that are typically outside this barrier [36,37]. This triggers an acute immune response from both microglia and astrocytes [38–40], which is then followed by chronic inflammation and neural degeneration around the implant [35,41,42]. These reactions can cause neuronal death and neurite degeneration and result in the formation of a tight glial sheath that blocks the electrical current flow for recording and stimulation [43]. Persistent leakage of the BBB can occur and may contribute to the accumulation of neurotoxic factors that negatively impact neuronal health and device performance [44]. It is also important to note that a significant amount of implantation

variability is observed [26,37,45,46]. As a result, the complex causal mechanisms behind device failure remain poorly understood.

The magnitude of the tissue response following device insertion could be influenced by a wide range of physical characteristics [35,47] including the surface and bulk properties of the device. Surface factors include hydrophilicity [9–11,48], texture [49,50] and presence or absence of bioactive molecules [51–53]. Bulk properties include size and geometry of the device [47,48,54–56] as well as the stiffness of the implanted materials [57]. Current neural probes are fabricated with very rigid materials with a high Young's modulus (E) such as tungsten (E = 400 GPa), silicon (E = 200 GPa), polyimide (E = 3 GPa) or parylene C (E = 2–5 GPa), while the brain tissue is very soft (E = 0.4–15 kPa) [58–61]. The enormous elastic modulus mismatch could contribute to "frustrated phagocytosis" [62–64] and exacerbate friction-induced stress under micromotion [38,57,65–67]. Furthermore, pro-inflammatory interleukin-1β (IL-1β) is shown to be upregulated by increased mechanical strain [68], which impairs the chronic performance of *in vivo* MEAs [34,64]. The glial scar, neuronal health and overall cellular response at the electrode-tissue interface are all negatively impacted by the mechanical mismatch between the implant and the brain tissue [34,43,63,69,70]. Moreover, stiff implants with delicate designs cannot adapt to normal tissue deformations as occurs with any implant, another factor that may lead to device failure from material fatigue and degradation [23].

Finite element modeling predicts that softer materials for neural implants can reduce the mechanical damage at the device-tissue interface and the micromotion-induced strain [57,66]. For this reason, compliant materials [71,72] and mechanically-adaptive materials [73,74] have been evaluated in both MEA shanks [45,75] and electrode coating materials [76]. Despite efforts to increase the softness and flexibility of *in vivo* MEAs, the Young's modulus of previously studied implants was only reduced to 5 MPa [77], 12 MPa [78], or 15 MPa [79]. To develop a softer implant that more closely mimics the mechanical properties of brain tissue, we fabricated ultra-soft microwires. The electrically conducting core of the microwire is made with a poly(3,4-ethylenedioxythio phene)-poly(ethyleneglycol) copolymer [PEDOT-PEG] with poly (dimethylsiloxane)[PDMS] elastomer; the electrically insulated outer coating is made of fluorosilicone [80]. The complete microwire electrode had a Young's modulus of 974 kPa and the ratio of PEDOT/PDMS was optimized for sufficient conductivity while maintaining the flexibility of the material [80].

Due to the difficulty of precisely implanting flexible devices into a target tissue location with currently available techniques, most recent flexible electrode arrays have been studied only *in vitro* [71,81] or via surface electrical recording and stimulation [75,82,83]. Several methods have been developed to deliver soft and flexible microdevices into neural tissue [71,84]. In addition, the mechanical stiffness of implants can be controlled and adapted depending on the condition of the implants [78]. In this study, we used a stiff shuttle to support and guide the microwire to the target location. The shuttle was made of a stiff needle that detached from the implant *in vivo* after precise targeting to the designated brain region.

Here, we report on the *in vivo* biocompatibility of our ultrasoft wire implants in the rodent brain after 1 and 8 weeks with comparisons to tungsten microwires, commonly used in

neural electrode arrays. To accurately assess the mechanical effect of these soft wires on the brain tissue response over control implants, both types of implants were designed to have similar geometry and surface chemistry. In addition to the common quantitative immuno-histochemical analysis on inflammation, glial scaring, BBB injury, and neuronal health and density [85], a novel automated cell shape and strain analysis was developed which demonstrates the striking difference in neuronal cell shape and tissue strain around the soft and stiff implants. Lastly, neural stimulation was performed in rat subthalamic nucleus (STN) to demonstrate the functionality of the soft electrodes for DBS applications [86,87].

2. Methods

2.1. Fabrication of electrodes

The implantable conducting elastomer microwire was reported in our previous study [80]. The fabrication process is briefly described as follows:

1. The soft conducting wires were made by extruding a blend of PEDOT-PEG conducting polymer (Aedotron™ C3, TDA Research Inc.) and polydimethylsiloxane (MED6607, NuSil Technology) through a 29G syringe needle. The wires were sputter-coated with gold along the shaft to increase the conductivity. Then, the wires were dip-coated up to 5 times to build an approximately 5-μm-thick layer of fluorosilicone (MED6655, NuSil Technology) along the outer surface that insulated the125-μm-diameter soft wire. The wire was trimmed at both ends with a razor to expose the conductive tips with active area of 12,270 μm^2 (one exposed end shown in inset of Fig. 1).

2. Standard tip tungsten microelectrodes with 127 μm diameter (MicroProbes, Gaithersburg, MD) were used as controls. To match the surface chemistry, the tungsten wires were dip-coated with a 380 nm thick fluorosilicone layer (resulting in a final outer diameter of 127.76 μm). After coating, tungsten electrodes were cut with wire cutters to match the squared-off tip profile of the soft wires.

The soft polymer wire had a Young's modulus of E = 974 kPa, cross section area A of 12,270 μm^2, and a length L of 1.5 cm, thus the axial stiffness k of the wire defined by Eq. (1) was 0.797 N/m. With a Young's modulus of E = 400 GPa, a cross section and active area of 12,820 μm^2 and a length of 1.2 cm, the Tungsten wire has a stiffness of 0.427×10^6 N/m, which is six orders of magnitude higher than the ultrasoft polymer wire. The geometrically soft polymer wires and geometrically stiff or rigid tungsten wires are therefore referred to as soft and stiff wires throughout the remainder of this manuscript, respectively.

$$K = \frac{A * E}{L} \quad (1)$$

2.2. Fabrication of shuttles for implantation

Fig. 1 illustrates the shuttle fabrication steps and features to support implantation of wire electrodes. 3.8-cm long 27G hypodermic dental needles (Fen Dental, Hialeah, FL) were

used to make the insertion shuttles. The LuerLok hub was removed and the needle glued to a polyester polishing block using a UV-curable adhesive (#68 Norland Optical Adhesive, Edmund Optics). Block-mounted needles were hand-polished on a Buehler polishing wheel with a 20 μm diamond lap surface. This slowly removed the top portion of the hypodermic needle until the center hollow was exposed and subsequently thinned down to just past the axial mid-point. After physically releasing the needles from the adhesive, the semi-cylindrical opening was used to cradle the soft wires during insertion.

Microwires (both soft and stiff) and shuttles were treated with oxygen plasma [71] for 120 s immediately prior to implantation to increase the hydrophilicity of the surface. Wires were then glued into the shuttle cavity with a 45% wt. solution of PEG (average molecular weight = 1500 Dalton) in acetonitrile to build the implant assembly (Fig. 1). The PEG glue was designed to hold the soft wire and shuttle together during insertion but to quickly dissolve within about 30 s after implantation to enable removal of the shuttle while leaving the microelectrode in place (although tweezers were used to stabilize the soft wire microelectrode near the brain surface preventing it from being pulled out during extraction of the shuttle). To keep the trauma to the insertion site nearly the same, stiff wires were also glued to the shuttles. Tweezers were not needed to hold the stiff wire electrodes in place while removing the shuttle.

2.3. Surgical procedures for biocompatibility studies

10-week old male Sprague-Dawley rats (Charles River) weighing 300–350 g were utilized to evaluate the *in vivo* performance of soft wires in comparison to conventional stiff wires. Animals were anesthetized with 3.0% isofluorane in 0.8 L/min oxygen for 5 min prior to surgery and then maintained for the duration of the procedure at 2.25% isofluorane. Anesthesia level was monitored closely during the procedure by observing changes in respiratory rate, heart rate, body temperature (37.7 °C) and absence of the pedal reflex. Animals were placed in a stereotaxic frame and the hair removed over the incision site. In each animal, four wires were implanted, two soft wires were randomly implanted into the left or right hemisphere and two stiff wires were implanted into the contralateral hemisphere. Wires were at least 2 mm apart on the skull to prevent possible crosstalk between tissue reactions around each wire. Wires were implanted to target a depth of 8 mm from the cortical surface with the aid of a stainless steel half needle insertion shuttle glued to the wire with PEG as described above. Once implanted, the PEG dissolved allowing the shuttle to detach from the wire and be removed. This design was used to insert both soft and stiff wires. Blue light-curing dental cement was used to build a well on the craniotomies, and craniotomies were filled with Kwik-Sil with the wires protruding out of the dental cement wells. Protruding ends of the wires were tethered to the skull with dental cement. Screws were placed to anchor the head-cap. Acute (week-1, $n = 7$) and chronic (week-8, $n = 7$) time points were evaluated (the number of analyzed images per group varied due to either outlier removal or because multiple depths were analyzed per animal, thus the image n per group is listed in each figure). All surgical procedures were done in accordance with the guidelines outlined by the United States Department of Agriculture and approved by the Institutional Animal Care and Use Committee of the University of Pittsburgh. Animals were housed in

the facilities of the University of Pittsburgh, Department of Laboratory Animal Resources and given free access to food and water.

2.4. DBS with soft wires evokes electroencephalography (EEG) local field potential(LFP)

Animals were anesthetized with 3.0% isofluorane in 0.8 L/min oxygen and maintained at 2.25% isofluorane. Soft wires ($n = 2$) were implanted into the STN of rats (3.8 mm posterior to bregma, 2.5 mm lateral to midline, 8 mm deep from brain surface) through a craniotomy to perform DBS and evoke reliable EEG LFP signals as outlined in previous studies [86]. The dura mater was cut to prevent possible separation of the soft wire from the shuttle due to the high friction at the dura surface. The soft wire was delivered using the shuttle in order to evoke specific neural activity in the STN neural network. An EEG recording screw was placed on the motor cortex (+2.5 mm anterior to bregma, +2.5 mm lateral to midline) and the EEG ground screw was positioned above the cerebellum (0.8 mm posterior to lambda and 2.0 mm lateral to midline). First, an impedance spectrum of the soft wire was measured after the electrode was implanted in the STN using the stainless steel half needle as the counter electrode (Fig. 7A). The stainless steel half needle shuttle was retained in the tissue as the counter electrode to perform bi-polar stimulation. Cathodic leading bi-polar square-wave stimulation with 90 μA amplitude and 200 μs duration per phase was delivered at 130 Hz to evoke LFP in motor cortex. A total of 650 waveforms were averaged to obtain the mean evoked LFP from the stimulation. After one DBS experiment, the rat was immediately euthanized with intracardial potassium chloride injection and further stimulations were performed to validate that the evoked LFP response was not an artifact.

2.5. Histology

At the designated time points, animals were deeply anesthetized with a ketamine/xylazine cocktail (100/20 mg/kg) via the intraperitoneal (IP) cavity. Animals were then transcardially perfused with cold (4 °C) PBS followed by 4% (w/v) paraformaldehyde (PFA) in PBS. For soft wires, rongeurs were used to carefully remove the bone and dental cement and expose the craniotomy. Then the soft wires were cut with scissors above the brain surface. All stiff wires were extracted together with the headcaps. The majority of the soft wires were left in the brain during tissue processing and sectioning with the exception of 2 soft wires extracted for imaging of the wire surface. The brain was removed, post-fixed for up to 3 days and then equilibrated in 30% sucrose (used as a cryoprotectant) prior to freezing. Serial sections were cut at a 15 mm thickness. The preserved soft and stiff wires were glued on metal studs and sputtered with 3.5 nm Pd using a Cressington Sputter Coater. Wire surfaces were imaged under JSM 6330F SEM (Joel, Japan) for characterization of cell adhesion onto the electrode.

For immunofluorescence staining, tissue sections were stained at the same time for each antibody combination to minimize variability. Markers to visualize mature axons (1:500 rabbit anti-NF-200, Abcam, Cambridge, UK), microglia (1:500 rabbit anti-Iba1, Wako Chemicals USA, Richmond, VA), astrocytes/fibroblasts/endo thelial cells (1:500 anti-Vimentin, Clone V-9, Millipore, Billerica MA), astrocytes (1:500 rabbit anti-GFAP, Dako, Glostrup, Denmark), neuronal nuclei (1:500 mouse anti-NeuN, Millipore, Billerica MA), apoptotic cell death (cleaved caspase-3, 1:50 Asp175; Cell Signaling Technology, Boston, MA), L1(a kind gift from Dr. Carl Lagenaur) and blood-brain barrier injury (1:500 goat anti-

rabbit IgG Alexa 633 conjugated, Invitrogen, Carlsbad CA) (antibodies outlined in Table 1) were used.

Tissue sections were hydrated in PBS and non-specific binding blocked with 0.5% bovine serum albumin (BSA). Primary antibodies were then diluted in BSA and added for approximately 1 h. After washing with BSA, fluorophore-conjugated secondary antibodies (conjugated to Alexa Fluor 488, Alexa Fluor 568 or Alexa Fluor 633) diluted in BSA were added for approximately 1 h and Hoechst used as the nuclear stain. Fluoromount-G (Southern Biotechnology Associates, Birmingham, AL) was used for mounting and to preserve fluorescence. Negative controls lacking primary antibody or including the appropriate blocking peptide were included for each secondary antibody or primary antibody, respectively.

2.6. Quantitative tissue analysis

Confocal fluorescent microscopy was used to evaluate the cellular reactions associated with the implanted electrodes. Images were acquired using an Olympus Fluoview 1000 II Confocal Microscope (Olympus America, Center Valley, PA) at the Center for Biologic Imaging at the University of Pittsburgh. For each antibody, images were acquired using the same laser power, exposure time, and detector settings to reduce variability during data analysis. Images were centered on the implant site and multi-channel images were acquired simultaneously. Fluorescent images of the explanted wires were reconstructed from 11 z-stack images with a step size of 4.1 μm in order to compensate for the curved surface of the wire. Pixel-based image intensity analytics were performed using previously published custom MATLAB script I.N.T.E.N.S.I.T.Y. v2.0 [85].

Briefly, to prevent holes in the tissue (major blood vessels and/ or shuttle tracks) from artificially reducing the average activity-dependent fluorescence, background noise intensity thresholds were calculated from corresponding control images. To calculate the background noise intensity threshold, pixels with intensity greater than one standard deviation dimmer than mean pixel intensity were removed from the calculation. The threshold was then determined by calculating the pixel intensity of one standard deviation below the mean of the remaining pixel intensities. Bins with intensity values dimmer than average intensities of the control images were considered tissue "holes." Using MATLAB, the center of the shuttle track was identified on each image, after which the script generated masks of concentric rings. The average intensity for all pixels above the background noise intensity threshold in each bin was calculated and normalized against the background to calculate the Signal-to-Noise Intensity Ratio (SNIR) in each bin as outlined in Eq. (2);

$$\mathrm{SNIR} = \frac{\mathrm{AvgI}_{>T}}{\mathrm{AvgN}} \quad (2)$$

where $AvgI_{>T}$ is the mean Intensity of all pixels above the noise threshold ($>T$) in each bin, and $AvgN$ is the mean noise floor intensity. This means an SNIR of 1 represents the noise floor. Therefore, it is expected that the SNIR does not asymptote to 1 unless there is no

staining signal in the corresponding bin. Data were averaged for each implant type and time point, and then reported as mean ± standard error.

2.7. Quantification of mechanical strain-induced cell deformation

To quantitatively assess the cell body shape deformation caused by the presence of a nearby foreign body (i.e., microelectrode), NeuN images were pre-processed and the cell shape was extracted using custom MATLAB scripts. To enhance cell shape recognition and reduce artifact-related false positives, images were flattened using a custom MATLAB script. First, image noise thresholds were established as with the I.N.T.E.N.S.I.T.Y. Analyzer v2.0 to create a mask to remove holes in the tissue. Next, a two-dimensional discrete Fourier Transform was applied over the remaining region and the zero-frequency component shifted to the center of the image. Once the image was flattened, the longer and shorter axes of the cell were determined by the program; the angle between the longer axis of the cell and the radial line from implant center to cell center was utilized to determine the direction of cell shape deformation. This angle was termed the cell elongation angle (CEA) and indicated the direction in which the cell body undergoes the most strain. That is, an angle near 90° indicates that the cell is most affected by mechanical strain from the radial direction outward from the implant. Conversely, a CEA near 0° indicates that the strain occurs predominantly from the tangential direction of the center-out line. The extent of cell body shape deformation was defined as the cell shape strain index (CSSI) as described in Eq. (3):

$$\text{CSSI} = \frac{\Delta L}{L_0} = \frac{(b - a)}{\frac{(b+a)}{2}} \quad (3)$$

where b is the length of the longer axis of the cell as defined in an elliptical shape, and a is the length of the shorter axis. ΔL represents the mechanical strain that a neuronal nuclei experiences, while L_0 estimates the mean diameter of the neuronal nuclei in the absence of strain. The mechanical strain associated with probe volume as well as the relationship between distance from the implant and CEA were determined.

2.8. Statistics

In all analyses the error bars represent the standard error of the sample. For cell number analysis, a two-sample T-test was performed to compare the differences between soft and stiff wires. For the cell shape deformation analysis with CEA and CSSI comparisons, Wilcoxon rank sum tests were performed to compare the two groups. For all tests, a p value < 0.05 indicated a statistically significant difference.

3. Results

3.1. Sub-chronic and chronic inflammatory tissue response

In order to evaluate the inflammatory tissue response and axonal damage associated with the implanted microelectrodes, the amount and distribution of microglia (Iba-1), astrocytes (GFAP) and axons (NF-200) were visualized. The soft wire tissue interface was well-preserved (Fig. 2) as soft wires were not explanted prior to sectioning of the fixed brain. On

the other hand, even though the stiff wires are circular in cross section and the diameter closely mimics the soft wire, the holes in the tissue sections are often irregular in shape (Fig. 2). Since stiff wires had to be extracted before tissue processing and fixation, tissue friction during explantation and the slight stretching of the brain slices during mounting could cause the distortion. The fixation process and the sucrose dehydration process could also each contribute to the distortion. At the week-1 time point, less glial activation was observed around soft wires as compared to stiff wires (Fig. 2, Compare E vs. F and I vs. J) although no statistical significance was noted (Fig. 2, S and U). The NF200 images demonstrate the same feature (Fig. 2, Compare A vs B) but yielded statistically significant differences in two quantified bins (Fig. 2, Q). This difference diminished at week-8 for NF200 intensity (Fig. 2, R). The inflammatory response around both types of implants was distributed over a relatively large region around each implant, indicating that the soft wire implants do not significantly reduce the acute tissue response. This is to be expected as both experimental and control tissues were damaged by the shuttle and at 7 days the stab wound may not be fully recovered. However, at week-8, a binned Iba-1 staining intensity reduction as much as 18.9% was observed around soft wires compared to the stiff ones (Fig. 2, G vs. H) and the area associated with the glial sheath was decreased when compared to that around the stiff implants (Fig. 2, K vs. L). If a GFAP relative intensity of 2 is used as the threshold for defined inflammation, at week-8 soft wires had 17 bins over this threshold while stiff wires had 26 bins over this threshold, yielding a striking 49.9% reduction in glial sheath area. These differences were statistically significant at distances within 100 μm of the interface (Fig. 2, T and V) and a much greater difference was observed in GFAP intensity. In addition, the intensity of GFAP and Iba-1 staining immediately around the soft wire implants is similar to the intensity observed in healthy tissue (i.e., at locations far from the implant site) (Fig. 2, G and K) which suggests an interface that does not continue to elicit an inflammatory response at this longer time point. In comparison, significant glial scarring consisting of both microglia and astrocytes formed around stiff implants as previously reported [41,52] (Fig. 2, H and L).

3.2. Neuronal density and health around the implant

To characterize the extent of neuronal loss near the implant, NeuN staining was combined with staining for activated caspase-3 to identify neurons undergoing programmed cell death via apoptosis [6]. Only a small number of apoptotic neurons indicated by colocalization of NeuN and caspase-3 were observed in all groups examined (Table 1), while a much larger number of non-neuronal cells were positive for caspase-3 (Fig. 3 A–D). Neuron numbers were quantified with automated MATLAB script. At week-1, the cell density around the soft implants was the same as for the stiff implants (Fig. 3, M). At week-8, however, the number of neurons around soft implants was significantly higher than those around the stiff implants at distances of 60–90 and 120– 210 μm. The neuron density around the soft implants between 90 and 120 μm still demonstrated a clear trend of increase compared to the stiff implants, although not statistically significant. The density of neurons can be highly variable according to many factors, including the heterogeneous neuron density in the brain region before implantation, the kill zone associated with the host tissue response, the slice thickness, the mechanical distortion of the implant-tissue interface as well as the bin size for post hoc analysis. Higher sample size may likely result in statistical significance in this 30

µm zone. Nevertheless, the NeuN positive cell numbers in all other quantified bins were higher around the soft implant than the stiff implant. This phenomenon combined with the sparse caspase-3 labeling suggests that the soft implants maintain a favorable environment for the survival of neurons compared to the stiff implants.

3.3. Cell deformation reflects different device-dependent strain

To better characterize the effects of implant softness on neuronal cells, cellular morphology was further characterized using both CEA and CSSI calculations. Three control images (from non implanted brain regions of three animals at a similar depth as the experimental groups) were analyzed. The mean CEA of control tissue was calculated to be 44.2 ± 0.6. For cells in an unaltered mechanical environment, CEA values ranging from 0–90° with a mean of 45° would be expected. The CSSI was determined to be 0.383 ± 0.006, reflecting the fact that the shape of the sectioned neuronal bodies are mostly non-circular. The CEA and CSSI from the control images gave the benchmark for non mechanically strained cell shape. Then experimental images were analyzed and quantified cells were binned every 30 µm beginning 30 µm from the tissue-electrode interface. The bins were determined such that the first bin had enough cells for quantification and statistical evaluation. At week 1, the CEA of cells closer to the soft wire implants showed higher CEA than the non implanted control and this difference disappears beyond 120 µm. (Fig. 4C). On the other hand, the cells around both soft and stiff implants showed significantly greater CSSI than the non implanted control of 0.383 ± 0.006 in most bins (Fig. 4D). Cells in the first quantifiable bin showed higher CEA in the presence of soft wire implants (Fig. 4C–D), possibly due to mechanical perturbations by the shuttle during soft wire implantation. Because soft wires were retained in the brain tissue by friction when shuttles were removed, tweezers were often used to stabilize the wire near the brain surface to retrieve the shuttle. During this process, additional strain was inevitably applied to cells surrounding the implant. This differs from what was done with the stiff wires as these wires could be held with greater stability during shuttle extraction. Interestingly, this effect was reversed at the week-8 time point (Fig. 4E–F) when both the CEA and CSSI are as much as 20.2% and 31.6% higher in the presence of stiff wires than in the presence of soft wires, respectively. This suggests that cells near soft wires eventually recover from the initial implant strain while cells near stiff wires are persistently deformed over the course of these experiments. The CSSI difference between the two groups was roughly consistent at week-1 and week-8, however, the difference was much great at week-8 with a statistical p-value as small as $4.79 * 10^{-13}$.

3.4. BBB injury related inflammation

We also examined the distribution of vimentin-positive cells (fibroblasts and glia cells), neural adhesion molecule L1 and the extent of blood-brain barrier (BBB) injury using IgG staining. Interestingly, the extent of BBB disruption was similar at week-1 for both implants but greater at week-8 with the stiff implants (Fig. 5, K vs L, and V). Furthermore, BBB leakage caused by the stiff implant is higher at week-8 than week-1, suggesting that the sustained mechanical disruption of the neural tissue by the tethered stiff implant results in persistent and aggravated BBB leakage. At the week-1 time point, the intensity of both Vimentin and L1 are higher around the stiff implant both nearby and far from the electrode-tissue interface (Fig. 5, Q and S). At week-8, Vimentin and L1 again showed a much higher

intensity near the stiff wires but the response zone is more confined to implants (Fig. 5R, T and V). Vimentin has been extensively used as a marker for inflammatory foreign body response while L1 has been shown to upregulate following implantation injury [6]. Taken together, all results indicate the superior performance of soft wires in facilitating the healing of tissue near the implants.

3.5. Explanted wire and tissue integration

Neurons (β-tubulin III), microglia (Iba-1), and astrocytes (GFAP) were labeled to qualitatively evaluate the types of tissue attached to the soft wires and tungsten controls. Note only 1 (week-1) and 3 (week-8) soft wires were removed due to loose headcaps which separated from the skull during brain dissection; the remaining soft implants were intentionally left in the brain. Therefore, quantification is not possible. At both week-1 and week-8 time points, a uniformly distributed layer of cells, majority of which are neurons, were found on soft wires (Fig. 6, E and G). In comparison, sparsely-distributed cells were located along the surface of stiff wires (Fig. 6, B, D, F, H, J, L, N and P). This result clearly indicates that soft wires greatly improve neural tissue integration compared to the control stiff wires. Scanning electron microscopy (SEM) examination of the wires following immunohistochemistry evaluation confirmed this same trend (Fig. 6, Q-T). The stripe pattern of insulation material on the stiff wires was exposed on the majority of the surfaces examined (Fig. 6, S and T) while the surface of the soft wires was covered by cells (Fig. 6, Q and R). The extent of cellular coverage was most prominent when wires were explanted at chronic time points (Fig. 6, R) in part because of the progressive condensation of the glial sheath around the implant. These results suggest that neural tissue integration is greatly improved with soft wire implants as compared to control wires.

3.6. Neural stimulation with soft microwires

To validate the *in vivo* electrical connectivity of the soft electrode, the electrochemical impedance spectrum was characterized in the rodent brain. Electrochemical impedance spectroscopy measures the resistance of current flow between the implanted electrode through the targeted neural tissue to the ground [24,43]. The impedance modulus of the implanted soft wire was maintained at a functional range around 41 kOhm at the physiologically relevant frequency of 1000 Hz; Fig. 7A shows that the soft wire has the proper range of impedance and a smooth phase angle curve which indicates that it is a satisfactory condition. In fact, both insulation cracking and excessive fluid infiltration would lead to low electrode impedance, while a damaged electrical connection or a small de-insulated surface would cause high electrode impedance and noisy impedance phase angle.

To further functionally validate the soft electrode for electrical stimulation and neuromodulation, a standard DBS stimulation experiment in rat STN was conducted. The stimulation paradigm was applied through the soft wire electrode and the evoked activity was recorded by an EEG skull screw over the motor cortex [86]. The latency of the evoked neural LFP response (Fig. 7B; blue asterisk) following the electrical stimulation artifact (Fig. 7B; red asterisks) was in accordance with those previously reported [86]. DBS in the STN using the soft wire microelectrodes was able to evoke high amplitude EEG LFP signals in the ipsilateral motor cortex indicating functional viability *in vivo* (Fig. 7B).

4. Discussion

In this study, we characterized the acute and chronic tissue response to novel ultrasoft elastomeric microwire electrodes. Qualitatively, there is no adverse effect observed from the soft wire which contains several novel materials that have not been tested in the brain before. In general, the soft implants perform the same as or better than the commonly used tungsten wires. Based on these results, we conclude that the novel implant material is biocompatible when implanted in the brain tissue for at least 8 weeks.

Our hypothesis was that the softness and flexibility of the implant would significantly reduce the inflammatory tissue response and improve neuronal survival and health around the implant. To definitively prove this hypothesis, the diameter and surface chemistry of the implants were kept similar, enabling this study to specifically investigate the mechanical influence from other factors that could impact tissue response. Several studies have tried to compare the neural tissue reactions of flexible versus stiff implants, but these studies failed to control for the size of the implants or surface chemistry or both, making it difficult to draw conclusions [88,89].

The low elastic modulus of the soft wires enabled *in situ* histo-logical characterization of the intact electrode-tissue interface as the tissue could be sectioned with the microelectrode in the tissue. This property was extremely beneficial for direct characterization of cell morphology and the inflammatory tissue response immediately adjacent to the implant. The stiff implants, on the other hand, had to be removed before sectioning, and this inevitably destroyed the immediate interface. To compensate, explant analysis was done to obtain a full understanding of the electrode-tissue integration. 1–2 soft wires per group were intentionally removed during dissection and characterization of these wires provided a comprehensive comparison between soft and stiff wires. These analyses indicate that the soft wire implants greatly enhance electrode-tissue integration and enable the adherence of neurons. An intimate integration would eliminate the relative movement between the implant and host tissue thereby reducing mechanical shearing and strain induced inflammation [66].

4.1. Inflammatory tissue response is mitigated by implant softness and flexibility

At earlier time points (i.e., week-1), both soft and stiff wires have similar levels of glial activation with only slight improvements observed with soft microelectrodes (Fig. 2, Q and S). Since the implantation of both implant types included stainless steel shuttles, the magnitude and type of initial tissue injury caused by the surgery was similar. The inflammation observed around the implants at week-1 are largely influenced by this acute stab wound injury, making it difficult to assess the mechanical effect of the different wires [41]. At week-8, when the stab wound influence is minimized, the results clearly demonstrate that our novel soft wire implants elicit reduced microglial (Fig. 2G and T) and astrocyte (Fig. 2K and V) activity. This supports the hypothesis that soft wires can greatly ameliorate the progressive development of gliosis around the implant. Since both implants were tethered on the skull, the metal implants with 10^6 time higher device stiffness will generate significant micromotion relative to the brain tissue as the animal moves, while the more flexible polymer implants are likely to reduce mechanical strain experienced by the brain tissue leading to a minimized inflammatory response. Moreover, neuronal survival and

health are significantly higher at the vicinity of the soft implants than the stiff implants at week-8 (Fig. 3, N). This indicates that our novel soft wires not only reduce the inflammatory response but positively impact neurons as well. Another mechanical difference between the two implants is the bulk material softness. It was known that different cell types respond differently to different mechanical moduli. Glial cells and fibroblasts prefer to grow on stiff substrate while neurons prefer soft substrates [90–93]. Therefore, the material stiffness may be another factor that results in the differential cellular response around the implants.

4.2. BBB injury and tissue repair

At week-1, the intensity increase of vimentin and L1 around the stiff implant extended far beyond the electrode-tissue interface (Fig. 5Q and S), indicating a wide range of cellular responses, while the reactive zone of soft implants is much reduced. On the other hand, the sub-chronic BBB injury indicated by IgG reactivity was more confined to the interface of both implant types. Therefore, we suspect that mechanisms other than inflammatory molecules leaking out of the BBB contributed to the wide activation of cellular responses. The lateral pressure from insertion of the shuttle and the micromotion of stiff wires may be transmitted across a broader range and result in a larger area of cellular responses [42,94]. At week-8, the increase in intensity of IgG reactivity is more confined for the soft implants, which correlates with the Vimentin and L1 staining, suggesting recovery of the BBB and successful healing. On the other hand, the stiff implants show increased IgG intensity, Vimentin 100 μm away from the implants, indicating chronic BBB leakage and persistent inflammation from the stiff implants even at week-8. Possibly because stiff wire continuously exert strain to adjacent tissue through micro-motion and up regulation of pro-inflammatory cytokines [35], while the soft wire adapt in its shape to dampen or even remove the pressure caused by micromotion.

4.3. Mechanical mismatch directly impacts the local cellular microenvironment

We postulate that when traditional stiff devices are used a significant amount of strain is caused by the horizontal displacement of the brain against the skull-anchored implant [88,89,95,96] while soft wires can dampen this effect [88]. In the representative images, the asymmetrical distribution in the cell shape distortion (Fig. 3F and H) could possibly be explained by a previous study reporting that a rigid cylindrical implant tethered to the skull caused oval scarring [97]. The author suggested the principle direction of brain movement relative to the skull of freely moving rodents may strongly influence the tissue response and the principle direction of brain movement caused more pressure to the cell body shape towards that direction [98]. Our analyses using automated algorithms confirmed that the neurons around the stiff implant had a much higher CSSI than those around the soft wires, and the CEA of cell body deformation was well aligned with predicted strain direction. While not all neuronal nuclei are naturally spherical, the large number of cells (N = 12,217) in this *meta*-analysis provides evidence of dramatic mechanical strain in the tissue from the accommodation of the probe volume in the presence of the stiff wire, confirming previous observations in acute studies [34,35]. This indicates that more compliant materials (i.e., those that more closely match the mechanical properties of the target tissue) may promote tissue equilibration following the probe volume-induced strain during and after the insertion as postulated in our previous study [80]. Fig. 6 demonstrated that tissue integration was

greatly improved in the presence of the soft wire as compared to the stiff wire. Better electrode tissue integration with soft wires could minimize the relative movement between the wire implant and the tissue and reduce the mechanical distortion forces exerted on nearby cell bodies during brain micromotion. As a result, little distortion in cell shape was observed around the soft implant. The reduced longitudinal cell body strain caused by the lower elastic modulus may improve chronic recording performance of neural implants due to the healthier cellular environment for neurons. This hypothesis will be directly evaluated in future chronic electrophysiological studies. The completeness and depth of the cell body deformation analysis with our novel automated cell shape analysis technique is impossible or hardly tractable with any conventional manual or even semi-automated image analysis algorithms. The further utilization of this technique in combination with novel automated image collection techniques could significantly accelerate the discovery of hidden mechanisms in complex biological systems.

4.4. Neural stimulation capability of the ultrasoft electrodes

Neural implant tissue compatibility and functionality are not always highly correlated [34,99,100]. Therefore, validating the functional performance of novel neural electrode designs is critical for future applications. In Fig. 7A, the *in vivo* impedance phase was maintained very near 0°, indicating that the resistivity of the electrode dominates the impedance at the electrode-tissue interface, a characteristic of the conducting polymer electrodes. This and the impedance modulus profile were clear indications that the soft wire was electrically functional *in vivo* and did not undergo any breakage or de-insulation. In Fig. 7B, the implanted soft wire successfully evoked strong LFP in the ipsilateral motor cortex, but the LFP peak number and shape is more complex compared to previous bipolar biphasic stimulation studies [86]. This is probably because the stimulation not only evoked a primary EEG LFP response by stimulating STN, but also evoked neural activity along the shank of the insertion shuttle used as the counter electrode. Future experiments with a bi-polar stimulation electrode design will improve the spatial specificity of neural stimulation. High frequency STN neural stimulation near 130 Hz is used clinically for the treatment of Parkinson's Disease (PD) as well as other episodic neural disorders like epilepsy. The degradation of DBS effectiveness over time may occur, at least in part, because of the chronic tissue response and replacement of conventional metal lead electrodes with soft wire implants could enhance the longevity of these devices. Utilizing soft wire materials in other implantable medical devices like cochlear implants and cardiac pacemakers may benefit from this improved tissue response as well.

4.5. Possible future development

Although improving chronic recording and stimulation is the ultimate goal, the focus of this manuscript is on the histological response to test the hypothesis that implant stiffness plays a critical role in inflammatory brain tissue response. The reduced foreign body response towards these soft implants demonstrates great promise for chronic neural interface applications. Despite the promising results obtained in this study, these novel soft microelectrodes require further improvement and testing before being used broadly in chronic neural recording and stimulation applications. First, longer term functional studies evaluating stability of the device composed of the novel materials *in vivo* will be necessary.

Secondly, the current dimensions of the wire are small enough for DBS, but further miniaturization will be necessary for microstimulation and single unit recording. Furthermore, methods need to be developed to fabricate multi-channel devices. In addition, conducting polymer and nanomaterial modifications of the electrode sites to improve neural recording specificity and long-term quality can greatly expand the versatility of this device [25,49,101]. Additional modifications to include bioactive coatings that promote neuronal health and reduce acute inflammation may further improve electrode tissue integration [51,53,102–105].

5. Conclusions

The chronic brain tissue response to ultrasoft conducting elastomer-based microwire neural electrodes was examined and compared to conventional stiff implants with the same surface chemistry and nearly identical dimensions. The soft wire was successfully inserted into the brain with the facilitation of a stiff shuttle and water dissolvable PEG glue. Our results indicate the following: 1) neurons at the interface of the soft electrodes showed normal morphology and much less mechanical strain-induced deformation; 2) less inflammatory gliosis was observed near the soft electrodes compared to the stiff ones; 3) significantly less chronic BBB injury and associated inflammatory response was caused by soft implants; 4) soft wires better integrated with host tissue compared to stiff wires as demonstrated by tightly bonded neurons and other cells on the explanted surface; and 5) the soft wires are effective in stimulating STN to evoke LFP in motor cortex for potential treatment of Parkinson's Disease.

Acknowledgments

References

1. Schwartz AB, Cui XT, Weber DJ, Moran DW. Brain-controlled interfaces: movement restoration with neural prosthetics. Neuron. 2006; 52(1):205–220. [PubMed: 17015237]

2. Wolpaw JR, Birbaumer N, McFarland DJ, Pfurtscheller G, Vaughan TM. Brain-computer interfaces for communication and control. Clin. Neurophysiol. 2002; 113(6):767–791. [PubMed: 12048038]

3. Schwartz AB. Cortical neural prosthetics. Annu. Rev. Neurosci. 2004; 27:487–507. [PubMed: 15217341]

4. Andersen RA, Hwang EJ, Mulliken GH. Cognitive neural prosthetics. Annu. Rev. Psychol. 2010; 61(169–90):C1–C3.

5. Wang W, Collinger JL, Degenhart AD, Tyler-Kabara EC, Schwartz AB, Moran DW, Weber DJ, Wodlinger B, Vinjamuri RK, Ashmore RC, Kelly JW, Boninger ML. An electrocorticographic brain interface in an individual with tetraplegia. PLoS ONE. 2013; 8(2):e55344. [PubMed: 23405137]

6. Kolarcik CL, Catt K, Rost E, Albrecht IN, Bourbeau D, Du Z, Kozai TD, Luo X, Weber DJ, Tracy Cui X. Evaluation of poly(3,4-ethylenedioxythiophene)/carbon nanotube neural electrode coatings for stimulation in the dorsal root ganglion. J. Neural Eng. 2015; 12(1):016008. [PubMed: 25485675]

7. Nicolelis MA. Actions from thoughts. Nature. 2001; 409(6818):403–407. [PubMed: 11201755]

8. Kozai TD, Vazquez AL. Photoelectric artefact from optogenetics and imaging on microelectrodes and bioelectronics: new challenges and opportunities. J. Mater. Chem. B. 2015

9. Hochberg LR, Serruya MD, Friehs GM, Mukand JA, Saleh M, Caplan AH, Branner A, Chen D, Penn RD, Donoghue JP. Neuronal ensemble control of prosthetic devices by a human with tetraplegia. Nature. 2006; 442(7099):164–171. [PubMed: 16838014]

10. Wodlinger B, Downey JE, Tyler-Kabara EC, Schwartz AB, Boninger ML, Collinger JL. Ten-dimensional anthropomorphic arm control in a human brain-machine interface: difficulties solutions and limitations. J. Neural Eng. 2015; 12(1):016011. [PubMed: 25514320]

11. Collinger JL, Wodlinger B, Downey JE, Wang W, Tyler-Kabara EC, Weber DJ, McMorland AJ, Velliste M, Boninger ML, Schwartz AB. High-performance neuroprosthetic control by an individual with tetraplegia. Lancet. 2013; 381(9866):557–564. [PubMed: 23253623]

12. Collinger JL, Kryger MA, Barbara R, Betler T, Bowsher K, Brown EH, Clanton ST, Degenhart AD, Foldes ST, Gaunt RA, Gyulai FE, Harchick EA, Harrington D, Helder JB, Hemmes T, Johannes MS, Katyal KD, Ling GS, McMorland AJ, Palko K, Para MP, Scheuermann J, Schwartz AB, Skidmore ER, Solzbacher F, Srikameswaran AV, Swanson DP, Swetz S, Tyler-Kabara EC, Velliste M, Wang W, Weber DJ, Wodlinger B, Boninger ML. Collaborative approach in the development of high-performance brain-computer interfaces for a neuroprosthetic arm: translation from animal models to human control. Clin. Transl. Sci. 2014; 7(1):52–59. [PubMed: 24528900]

13. Wood SM, Jarratt JA, Barker AT, Brown BH. Surface electromyography using electrode arrays: a study of motor neuron disease. Muscle Nerve. 2001; 24(2):223–230. [PubMed: 11180205]

14. Chong SA, Benilova I, Shaban H, De Strooper B, Devijver H, Moechars D, Eberle W, Bartic C, Van Leuven F, Callewaert G. Synaptic dysfunction in hippocampus of transgenic mouse models of Alzheimer's disease: a multi-electrode array study. Neurobiol. Dis. 2011; 44(3):284–291. [PubMed: 21807097]

15. Rouse AG, Stanslaski SR, Cong P, Jensen RM, Afshar P, Ullestad D, Gupta R, Molnar GF, Moran DW, Denison TJ. A chronic generalized bidirectional brain-machine interface. J. Neural Eng. 2011; 8(3):036018. [PubMed: 21543839]

16. Obeso JA, Olanow CW, Rodriguez-Oroz MC, Krack P, Kumar R, Lang E. A, Deep-brain stimulation of the subthalamic nucleus or the pars Interna of the globus pallidus in Parkinson's disease. N. Engl. J. Med. 2001; 345(13):956–963. [PubMed: 11575287]

17. Loddenkemper T, Pan A, Neme S, Baker KB, Rezai AR, Dinner DS, Montgomery EB Jr, Luders HO. Deep brain stimulation in epilepsy. J. Clin. Neurophysiol. 2001; 18(6):514–532. [PubMed: 11779965]

18. Mayberg HS, Lozano AM, Voon V, McNeely HE, Seminowicz D, Hamani C, Schwalb JM, Kennedy SH. Deep brain stimulation for treatment-resistant depression. Neuron. 2005; 45(5):651–660. [PubMed: 15748841]

19. Mallet L, Polosan M, Jaafari N, Baup N, Welter ML, Fontaine D, du Montcel ST, Yelnik J, Chereau I, Arbus C, Raoul S, Aouizerate B, Damier P, Chabardes S, Czernecki V, Ardouin C, Krebs MO, Bardinet E, Chaynes P, Burbaud P, Cornu P, Derost P, Bougerol T, Bataille B, Mattei V, Dormont D, Devaux B, Verin M, Houeto JL, Pollak P, Benabid AL, Agid Y, Krack P, Millet B, Pelissolo A, Group SS. Subthalamic nucleus stimulation in severe obsessive-compulsive disorder. N. Engl. J. Med. 2008; 359(20):2121–2134. [PubMed: 19005196]

20. Nicolelis MA, Dimitrov D, Carmena JM, Crist R, Lehew G, Kralik JD, Wise SP. Chronic multisite multielectrode recordings in macaque monkeys. Proc. Natl. Acad. Sci. U S A. 2003; 100(19): 11041–11046. [PubMed: 12960378]

21. Chestek CA, Gilja V, Nuyujukian P, Foster JD, Fan JM, Kaufman MT, Churchland MM, Rivera-Alvidrez Z, Cunningham JP, Ryu SI, Shenoy KV. Long-term stability of neural prosthetic control signals from silicon cortical arrays in rhesus macaque motor cortex. J. Neural Eng. 2011; 8(4): 045005. [PubMed: 21775782]

22. Wise KD, Anderson DJ, Hetke JF, Kipke DR, Najafi K. Wireless implantable microsystems: High-density electronic interfaces to the nervous system. Pleee. 2004; 92(1):76–97.

23. Kozai TD, Catt K, Li X, Gugel ZV, Olafsson VT, Vazquez AL, Cui XT. Mechanical failure modes of chronically implanted planar silicon-based neural probes for laminar recording. Biomaterials. 2015; 37:25–39. [PubMed: 25453935]

24. Kozai TD, Du Z, Gugel ZV, Smith MA, Chase SM, Bodily LM, Caparosa EM, Friedlander RM, Cui XT. Comprehensive chronic laminar single-unit, multi-unit, and local field potential recording performance with planar single shank electrode arrays. J. Neurosci. Methods. 2014; 242C:15–40.

25. Kozai T, Catt K, Du Z, Kyounghwan N, Srivannavit O, Haque RU, Seymour J, Wise K, Yoon E, Cui X. Chronic in vivo evaluation of PEDOT/CNT for stable neural recordings. IEEE Trans. Biomed. Eng. 2015

26. Williams JC, Rennaker RL, Kipke DR. Long-term neural recording characteristics of wire microelectrode arrays implanted in cerebral cortex. Brain Res. 1999; 4(3):303–313.

27. Ward MP, Rajdev P, Ellison C, Irazoqui PP. Toward a comparison of microelectrodes for acute and chronic recordings. Brain Res. 2009; 1282:183–200. [PubMed: 19486899]

28. Wang C, Brunton E, Haghgooie S, Cassells K, Lowery A, Rajan R. Characteristics of electrode impedance and stimulation efficacy of a chronic cortical implant using novel annulus electrodes in rat motor cortex. J. Neural Eng. 2013; 10(4):046010. [PubMed: 23819958]

29. Sillay KA, Rutecki P, Cicora K, Worrell G, Drazkowski J, Shih JJ, Sharan AD, Morrell MJ, Williams J, Wingeier B. Long-term measurement of impedance in chronically implanted depth and subdural electrodes during responsive neurostimulation in humans. Brain Stimul. 2013; 6(5):718–726. [PubMed: 23538208]

30. Lempka SF, Miocinovic S, Johnson MD, Vitek JL, McIntyre CC. In vivo impedance spectroscopy of deep brain stimulation electrodes. J. Neural Eng. 2009; 6(4):046001. [PubMed: 19494421]

31. Butson CR, Maks CB, McIntyre CC. Sources and effects of electrode impedance during deep brain stimulation. Clin. Neurophysiol. 2006; 117(2):447–454. [PubMed: 16376143]

32. Sillay KA, Chen JC, Montgomery EB. Long-term measurement of therapeutic electrode impedance in deep brain stimulation. Neuromodulation. 2010; 13(3):195–200. [PubMed: 21992832]

33. Johnson MD, Otto KJ, Kipke DR. Repeated voltage biasing improves unit recordings by reducing resistive tissue impedances. IEEE Trans. Neural Syst. Rehabil. Eng. 2005; 13(2):160–165. [PubMed: 16003894]

34. Kozai TD, Li X, Bodily LM, Caparosa EM, Zenonos GA, Carlisle DL, Friedlander RM, Cui XT. Effects of caspase-1 knockout on chronic neural recording quality and longevity: Insight into cellular and molecular mechanisms of the reactive tissue response. Biomaterials. 2014; 435(36): 9620–9634.

35. Kozai TD, Jaquins-Gerstl AS, Vazquez AL, Michael AC, Cui XT. Brain tissue responses to neural implants impact signal sensitivity and intervention strategies. ACS Chem. Neurosci. 2015; 6(1): 48–67. [PubMed: 25546652]

36. Rubin LL, Staddon JM. The cell biology of the blood-brain barrier. Annu. Rev. Neurosci. 1999; 22(1):11–28. [PubMed: 10202530]

37. Kozai TDY, Marzullo TC, Hooi F, Langhals NB, Majewska AK, Brown EB, Kipke DR. Reduction of neurovascular damage resulting from microelectrode insertion into the cerebral cortex using in vivo two-photon mapping. J. Neural Eng. 2010; 7(4):046011. [PubMed: 20644246]

38. Turner JN, Shain W, Szarowski DH, Andersen M, Martins S, Isaacson M, Craighead H. Cerebral astrocyte response to micromachined silicon implants. Exp. Neurol. 1999; 156(1):33–49. [PubMed: 10192775]

39. Roitbak T, Sykova E. Diffusion barriers evoked in the rat cortex by reactive astrogliosis. Glia. 1999; 28(1):40–48. [PubMed: 10498821]

40. Kozai TD, Vazquez AL, Weaver CL, Kim SG, Cui XT. In vivo two-photon microscopy reveals immediate microglial reaction to implantation of microelectrode through extension of processes. J. Neural Eng. 2012; 9(6):066001. [PubMed: 23075490]

41. Biran R, Martin DC, Tresco PA. Neuronal cell loss accompanies the brain tissue response to chronically implanted silicon microelectrode arrays. Exp. Neurol. 2005; 195(1):115–126. [PubMed: 16045910]

42. Kozai TD, Eles JR, Vazquez AL, Cui XT. Two-photon imaging of chronically implanted neural electrodes: sealing methods and new insights. J. Neurosci. Methods. 2016; 258:46–55. [PubMed: 26526459]

43. Williams JC, Hippensteel JA, Dilgen J, Shain W, Kipke DR. Complex impedance spectroscopy for monitoring tissue responses to inserted neural implants. J. Neural Eng. 2007; 4(4):410–423. [PubMed: 18057508]

Author Manuscript

Author Manuscript

Author Manuscript

Author Manuscript

44. Saxena T, Karumbaiah L, Gaupp EA, Patkar R, Patil K, Betancur M, Stanley GB, V R. Bellamkonda, The impact of chronic blood-brain barrier breach on intracortical electrode function. Biomaterials. 2013

45. Rousche PJ, Pellinen DS, Williams DP Jr, Pivin JC, Vetter RJ, Kipke DR. Flexible polyimide-based intracortical electrode arrays with bioactive capability. IEEE Trans. Biomed. Eng. 2001; 48(3):361–371. [PubMed: 11327505]

46. Kozai TD, Jaquins-Gerstl AS, Vazquez AL, Michael AC, Cui XT. Dexamethasone retrodialysis attenuates microglial response to implanted probes in vivo. Biomaterials. 2016; 87:157–169. [PubMed: 26923363]

47. Seymour JP, Kipke DR. Neural probe design for reduced tissue encapsulation in CNS. Biomaterials. 2007; 28(25):3594–3607. [PubMed: 17517431]

48. Kozai TD, Langhals NB, Patel PR, Deng X, Zhang H, Smith KL, Lahann J, Kotov NA, Kipke DR. Ultrasmall implantable composite microelectrodes with bioactive surfaces for chronic neural interfaces. Nat. Mater. 2012; 11(12):1065–1073. [PubMed: 23142839]

49. Du ZJ, Luo X, Weaver CL, Cui XT. Poly(3,4-ethylenedioxythiophene)-ionic liquid coating improves neural recording and stimulation functionality of MEAs. J. Mater. Chem. C. 2015; 3(25): 6515–6524.

50. Kozai, T., Alba, N., Zhang, H., Kotov, N., Gaunt, R., Cui, X. Nanostructured coatings for improved charge delivery to neurons. In: Vittorio, MD.Martiradonna, L., Assad, J., editors. Nanotechnology and Neuroscience: Nano-electronic, Photonic and Mechanical Neuronal Interfacing. Springer, New York; New York, NY: 2014. p. 71-134.

51. Kolarcik CL, Bourbeau D, Azemi E, Rost E, Zhang L, Lagenaur CF, Weber DJ, Cui XT. In vivo effects of L1 coating on inflammation and neuronal health at the electrode-tissue interface in rat spinal cord and dorsal root ganglion. Acta Biomater. 2012; 8(10):3561–3575. [PubMed: 22750248]

52. Azemi E, Lagenaur CF, Cui XT. The surface immobilization of the neural adhesion molecule L1 on neural probes and its effect on neuronal density and gliosis at the probe/tissue interface. Biomaterials. 2011

53. Eles JR, Vazquez AL, Snyder NR, Lagenaur CF, Murphy MC, Kozai TDY, Cui XT. Neuroadhesive L1 coating attenuates acute microglial attachment to neural electrodes as revealed by live two-photon microscopy. Biomaterials. 2017; 113:279–292. [PubMed: 27837661]

54. Khilwani R, Gilgunn PJ, Kozai TDY, Ong XC, Korkmaz E, Gunalan PK, Cui XT, Fedder GK, Ozdoganlar OB. Ultra-miniature ultra-compliant neural probes with dissolvable delivery needles: design, fabrication and characterization. Biomed. Microdevices. 2016; 18(6):97. [PubMed: 27778225]

55. Gilgunn, PJ., Khilwani, R., Kozai, TDY., Weber, DJ., Cui, XT., Erdos, G., Ozdoganlar, OB., Fedder, GK. An ultra-compliant, scalable neural probe with molded biodissolvable delivery vehicle, Micro Electro Mechanical Systems (MEMS); 2012 IEEE 25th International Conference on; 2012. p. 56-59.

56. Patel PR, Zhang H, Robbins MT, Nofar JB, Marshall SP, Kobylarek MJ, Kozai TDY, Kotov NA, Chestek CA. Chronic In Vivo Stability Assessment of Carbon Fiber Microelectrode Arrays. In Review. 2016

57. Subbaroyan J, Martin DC, Kipke DR. A finite-element model of the mechanical effects of implantable microelectrodes in the cerebral cortex. J. Neural Eng. 2005; 2(4):103–113. [PubMed: 16317234]

58. Fallenstein GT, Hulce VD, Melvin JW. Dynamic mechanical properties of human brain tissue. J. Biomech. 1969; 2(3):217–226. [PubMed: 16335085]

59. Miller K, Chinzei K, Orssengo G, Bednarz P. Mechanical properties of brain tissue in-vivo: experiment and computer simulation. J. Biomech. 2000; 33(11):1369–1376. [PubMed: 10940395]

60. Georges PC, Miller WJ, Meaney DF, Sawyer ES, Janmey PA. Matrices with compliance comparable to that of brain tissue select neuronal over glial growth in mixed cortical cultures. Biophys. J. 2006; 90(8):3012–3018. [PubMed: 16461391]

61. Lu YB, Franze K, Seifert G, Steinhauser C, Kirchhoff F, Wolburg H, Guck J, Janmey P, Wei EQ, Kas J, Reichenbach A. Viscoelastic properties of individual glial cells and neurons in the CNS. Proc. Natl. Acad. Sci. U S A. 2006; 103(47):17759–17764. [PubMed: 17093050]

62. Biran R, Martin DC, Tresco PA. The brain tissue response to implanted silicon microelectrode arrays is increased when the device is tethered to the skull. J. Biomed. Mater. Res. 2007; A82(1): 169–178.

63. Polikov VS, Tresco PA, Reichert WM. Response of brain tissue to chronically implanted neural electrodes. J. Neurosci. Methods. 2005; 148(1):1–18. [PubMed: 16198003]

64. Moshayedi P, Ng G, Kwok JC, Yeo GS, Bryant CE, Fawcett JW, Franze K, Guck J. The relationship between glial cell mechanosensitivity and foreign body reactions in the central nervous system. Biomaterials. 2014; 35(13):3919–3925. [PubMed: 24529901]

65. LaPlaca MC, Cullen DK, McLoughlin JJ, Cargill RS 2nd. High rate shear strain of three-dimensional neural cell cultures: a new in vitro traumatic brain injury model. J. Biomech. 2005; 38(5):1093–1105. [PubMed: 15797591]

66. Lee H, Bellamkonda RV, Sun W, Levenston ME. Biomechanical analysis of silicon microelectrode-induced strain in the brain. J. Neural Eng. 2005; 2(4):81–89. [PubMed: 16317231]

67. Neary JT, Kang Y, Willoughby KA, Ellis EF. Activation of extracellular signal-regulated kinase by stretch-induced injury in astrocytes involves extracellular ATP and P2 purinergic receptors. J. Neurosci. 2003; 23(6):2348–2356. [PubMed: 12657694]

68. Woodroofe MN, Sarna GS, Wadhwa M, Hayes GM, Loughlin AJ, Tinker A, Cuzner ML. Detection of interleukin-1 interleukin-6 in adult rat brain, following mechanical injury by in vivo microdialysis: evidence of a role for microglia in cytokine production. J. Neuroimmunol. 1991; 33(3):227–236. [PubMed: 1874973]

69. He, W., Bellamkonda, RV. A molecular perspective on understanding and modulating the performance of chronic central nervous system (CNS) recording electrodes. In: Reichert, WM., editor. Indwelling Neural Implants: Strategies for Contending with the In Vivo Environment. Boca Raton (FL): 2008.

70. Leach JB, Achyuta AK, Murthy SK. Bridging the divide between neuroprosthetic design tissue engineering and neurobiology. Front. Neuroeng. 2010; 2:18. [PubMed: 20161810]

71. Kozai TD, Kipke DR. Insertion shuttle with carboxyl terminated self-assembled monolayer coatings for implanting flexible polymer neural probes in the brain. J. Neurosci. Methods. 2009; 184(2):199–205. [PubMed: 19666051]

72. Patel PR, Na K, Zhang H, Kozai TD, Kotov NA, Yoon E, Chestek CA. Insertion of linear 8.4 mum diameter 16 channel carbon fiber electrode arrays for single unit recordings. J. Neural Eng. 2015; 12(4):046009. [PubMed: 26035638]

73. Capadona JR, Shanmuganathan K, Tyler DJ, Rowan SJ, Weder C. Stimuli-responsive polymer nanocomposites inspired by the sea cucumber dermis. Science. 2008; 319(5868):1370–1374. [PubMed: 18323449]

74. Ware T, Simon D, Liu C, Musa T, Vasudevan S, Sloan A, Keefer EW, Rennaker RL 2nd, Voit W. Thiol-ene/acrylate substrates for softening intracortical electrodes. J. Biomed. Mater. Res. B Appl. Biomater. 2014; 102(1):1–11. [PubMed: 23666562]

75. Khodagholy D, Doublet T, Gurfinkel M, Quilichini P, Ismailova E, Leleux P, Herve T, Sanaur S, Bernard C, Malliaras GG. Highly conformable conducting polymer electrodes for in vivo recordings. Adv. Mater. 2011; 23(36):H268–H272. [PubMed: 21826747]

76. Leleux P, Badier JM, Rivnay J, Benar C, Herve T, Chauvel P, Malliaras GG. Conducting polymer electrodes for electroencephalography. Adv. Healthcare Mater. 2014; 3(4):490–493.

77. Ware T, Simon D, Hearon K, Kang TH, Maitland DJ, Voit W. Thiol-click chemistries for responsive neural interfaces. Macromol. Biosci. 2013; 13(12):1640–1647. [PubMed: 24115484]

78. Harris JP, Capadona JR, Miller RH, Healy BC, Shanmuganathan K, Rowan SJ, Weder C, Tyler DJ. Mechanically adaptive intracortical implants improve the proximity of neuronal cell bodies. J. Neural Eng. 2011; 8(6):066011. [PubMed: 22049097]

79. Harris JP, Hess AE, Rowan SJ, Weder C, Zorman CA, Tyler DJ, Capadona JR. In vivo deployment of mechanically adaptive nanocomposites for intracortical microelectrodes. J. Neural Eng. 2011; 8(4):046010. [PubMed: 21654037]

80. Kolarcik CL, Luebben SD, Sapp SA, Hanner J, Snyder N, Kozai TDY, Chang E, Nabity JA, Nabity ST, Lagenaur CF, Cui XT. Elastomeric and soft conducting microwires for implantable neural interfaces. Soft Matter. 2015; 11(24):4847–4861. [PubMed: 25993261]

81. Blau A, Murr A, Wolff S, Sernagor E, Medini P, Iurilli G, Ziegler C, Benfenati F. Flexible, all-polymer microelectrode arrays for the capture of cardiac and neuronal signals. Biomaterials. 2011; 32(7):1778–1786. [PubMed: 21145588]

82. Kim DH, Viventi J, Amsden JJ, Xiao J, Vigeland L, Kim YS, Blanco JA, Panilaitis B, Frechette ES, Contreras D, Kaplan DL, Omenetto FG, Huang Y, Hwang KC, Zakin MR, Litt B, Rogers JA. Dissolvable films of silk fibroin for ultrathin conformal bio-integrated electronics. Nat. Mater. 2010; 9(6):511–517. [PubMed: 20400953]

83. Rodger DC, Fong AJ, Li W, Ameri H, Ahuja AK, Gutierrez C, Lavrov I, Zhong H, Menon PR, Meng E, Burdick JW, Roy RR, Edgerton VR, Weiland JD, Humayun MS, Tai Y-C. Flexible parylene-based multielectrode array technology for high-density neural stimulation and recording. Sensors Actuat. B: Chem. 2008; 132(2):449–460.

84. Felix S, Shah K, George D, Tolosa V, Tooker A, Sheth H, Delima T, Pannu S. Removable silicon insertion stiffeners for neural probes using polyethylene glycol as a biodissolvable adhesive. Conf. Proc. IEEE Eng. Med. Biol. Soc. 2012; 2012:871–874. [PubMed: 23366031]

85. Kozai TDY, Gugel Z, Li X, Gilgunn PJ, Khilwani R, Ozdoganlar OB, Fedder GK, Weber DJ, Cui XT. Chronic tissue response to carboxymethyl cellulose based dissolvable insertion needle for ultra-small neural probes. Biomaterials. 2014; 35(34):9255–9268. [PubMed: 25128375]

86. Dejean C, Hyland B, Arbuthnott G. Cortical effects of subthalamic stimulation correlate with behavioral recovery from dopamine antagonist induced akinesia. Cereb. Cortex. 2009; 19(5):1055–1063. [PubMed: 18787234]

87. Limousin P, Pollak P, Benazzouz A, Hoffmann D, Le Bas JF, Broussolle E, Perret JE, Benabid AL. Effect of parkinsonian signs and symptoms of bilateral subthalamic nucleus stimulation. Lancet. 1995; 345(8942):91–95. [PubMed: 7815888]

88. Nguyen JK, Park DJ, Skousen JL, Hess-Dunning AE, Tyler DJ, Rowan SJ, Weder C, Capadona JR. Mechanically-compliant intracortical implants reduce the neuroinflammatory response. J. Neural Eng. 2014; 11(5):056014. [PubMed: 25125443]

89. Sridharan A, Nguyen JK, Capadona JR, Muthuswamy J. Compliant intracortical implants reduce strains and strain rates in brain tissue in vivo. J. Neural Eng. 2015; 12(3):036002. [PubMed: 25834105]

90. Balgude AP, Yu X, Szymanski A, Bellamkonda RV. Agarose gel stiffness determines rate of DRG neurite extension in 3D cultures. Biomaterials. 2001; 22(10):1077–1084. [PubMed: 11352088]

91. Flanagan LA, Ju YE, Marg B, Osterfield M, Janmey PA. Neurite branching on deformable substrates. NeuroReport. 2002; 13(18):2411–2415. [PubMed: 12499839]

92. Georges PC, Janmey PA. Cell type-specific response to growth on soft materials. J. Appl. Physiol. 2005; 98(4):1547–1553. [PubMed: 15772065]

93. Lo C-M, Wang H-B, Dembo M, Wang Y-L. Cell movement is guided by the rigidity of the substrate. Biophys. J. 2000; 79(1):144–152. [PubMed: 10866943]

94. Bjornsson CS, Oh SJ, Al-Kofahi YA, Lim YJ, Smith KL, Turner JN, De S, Roysam B, Shain W, Kim SJ. Effects of insertion conditions on tissue strain and vascular damage during neuroprosthetic device insertion. J. Neural Eng. 2006; 3(3):196–207. [PubMed: 16921203]

95. Karumbaiah L, Norman SE, Rajan NB, Anand S, Saxena T, Betancur M, Patkar R, Bellamkonda RV. The upregulation of specific interleukin (IL) receptor antagonists and paradoxical enhancement of neuronal apoptosis due to electrode induced strain and brain micromotion. Biomaterials. 2012

96. Kim YT, Hitchcock RW, Bridge MJ, Tresco PA. Chronic response of adult rat brain tissue to implants anchored to the skull. Biomaterials. 2004; 25(12):2229–2237. [PubMed: 14741588]

97. Thelin J, Jorntell H, Psouni E, Garwicz M, Schouenborg J, Danielsen N, Linsmeier CE. Implant size and fixation mode strongly influence tissue reactions in the CNS. PLoS ONE. 2011; 6(1):e16267. [PubMed: 21298109]

98. Kohler P, Wolff A, Ejserholm F, Wallman L, Schouenborg J, Linsmeier CE. Influence of probe flexibility and gelatin embedding on neuronal density and glial responses to brain implants. PLoS ONE. 2015; 10(3):e0119340. [PubMed: 25790172]

99. Barrese JC, Rao N, Paroo K, Triebwasser C, Vargas-Irwin C, Franquemont L, Donoghue JP. Failure mode analysis of silicon-based intracortical microelectrode arrays in non-human primates. J. Neural Eng. 2013; 10(6):066014. [PubMed: 24216311]

100. McCreery D, Cogan S, Kane S, Pikov V. Correlations between histology and neuronal activity recorded by microelectrodes implanted chronically in the cerebral cortex. J. Neural Eng. 2016; 13(3):036012. [PubMed: 27108712]

101. Alba N, Du Z, Catt K, Kozai T, Cui X. In vivo electrochemical analysis of a PEDOT/MWCNT neural electrode coating. Biosensors. 2015; 5(4):618. [PubMed: 26473938]

102. Azemi E, Lagenaur CF, Cui XT. The surface immobilization of the neural adhesion molecule L1 on neural probes and its effect on neuronal density and gliosis at the probe/tissue interface. Biomaterials. 2011; 32(3):681–692. [PubMed: 20933270]

103. Cui X, Lee VA, Raphael Y, Wiler JA, Hetke JF, Anderson DJ, Martin DC. Surface modification of neural recording electrodes with conducting polymer/biomolecule blends. J. Biomed. Mater. Res. 2001; 56(2):261–272. [PubMed: 11340598]

104. Cui X, Martin DC. Electrochemical deposition and characterization of poly (3,4-ethylenedioxythiophene) on neural microelectrode arrays. Sensors Actuat. B: Chem. 2003; 89(1–2):92–102.

105. Cui X, Wiler J, Dzaman M, Altschuler RA, Martin DC. In vivo studies of polypyrrole/peptide coated neural probes. Biomaterials. 2003; 24(5):777–787. [PubMed: 12485796]

Statement of Significance

One critical challenge to the translation of neural recording/stimulation electrode technology to clinically viable devices for brain computer interface (BCI) or deep brain stimulation (DBS) applications is the chronic degradation of device performance due to the inflammatory tissue reaction. While many hypothesize that soft and flexible devices elicit reduced inflammatory tissue responses, there has yet to be a rigorous comparison between soft and stiff implants. We have developed an ultra-soft microelectrode with Young's modulus lower than 1 MPa, closely mimicking the brain tissue modulus. Here, we present a rigorous histological comparison of this novel ultrasoft electrode and conventional stiff electrode with the same size, shape and surface chemistry, implanted in rat brains for 1-week and 8-weeks. Significant improvement was observed for ultrasoft electrodes, including inflammatory tissue reaction, electrode-tissue integration as well as mechanical disturbance to nearby neurons. A full spectrum of new techniques were developed in this study, from insertion shuttle to *in situ* sectioning of the microelectrode to automated cell shape analysis, all of which should contribute new methods to the field. Finally, we showed the electrical functionality of the ultrasoft electrode, demonstrating the potential of flexible neural implant devices for future research and clinical use.
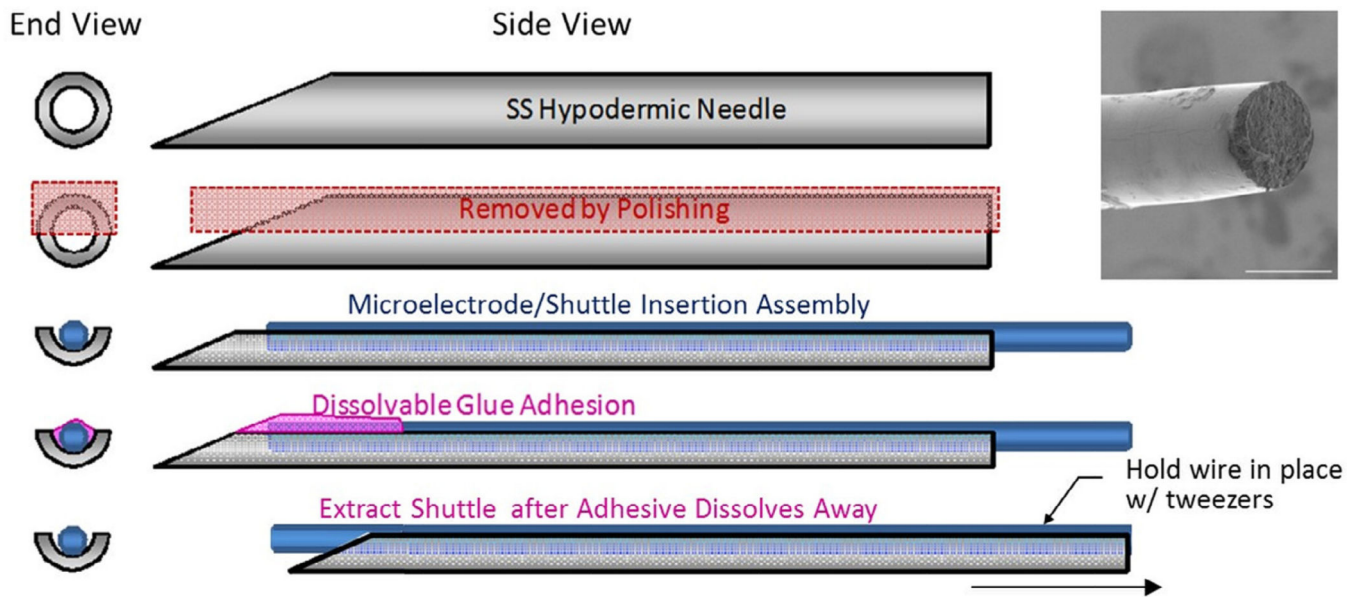
Fig. 1.

Illustration of fabricated parts, implant assembly, insertion and wire electrode release. From top: 1) Original needle; 2) Fabricated half-needle shuttle; 3) Mount soft/ stiff wire; 4) PEG facilitated assembly; 5) Wire detachment *in vivo*. Inset on top right corner: SEM image of fabricated soft wire tip. Scale bar = 100 μm.
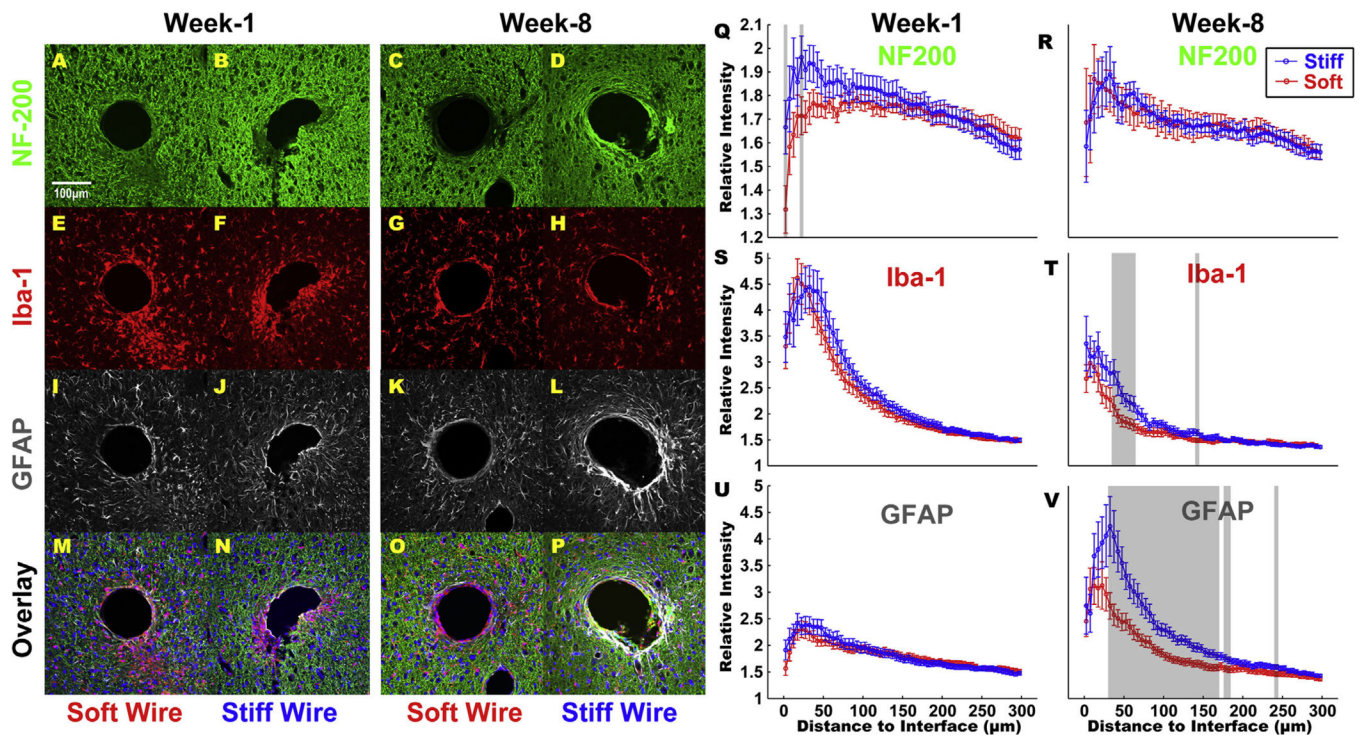
Fig. 2.
NF200, Iba-1 and GFAP expression around soft and stiff implants. NF200, Iba-1 and GFAP stain for axons, microglia and astrocytes, respectively. M-P are the overlay images including Hoechst. Groups of histology from left-most are soft wire at week-1, stiff wire at week-1, soft wire at week-8 and stiff wire at week-8. These groups are consistent through all immunohistochemistry figures. Scale bar = 100 μm. Q and R are the normalized intensity values for NF-200 expression at week-1 (animal n = 7, multiple samples from one animal, outliers removed according to 2*standard deviation, N = 42 histological samples quantified for soft wire, for stiff N = 42. All subsequent are denoted similarly.) and week-8(soft N = 34, stiff N = 38), respectively; S and T are normalized intensity values for Iba-1 expression at week-1(soft N = 45, stiff N = 46) and week-8(soft N = 34, stiff N = 35), respectively; U and V are normalized intensity values for GFAP expression at week-1(soft N = 45, stiff N = 43) and week-8(soft N = 33, stiff N = 37), respectively. Intensities are calculated 0 μm from the electrode-tissue interface until 300 μm away, with 5 μm bin size.
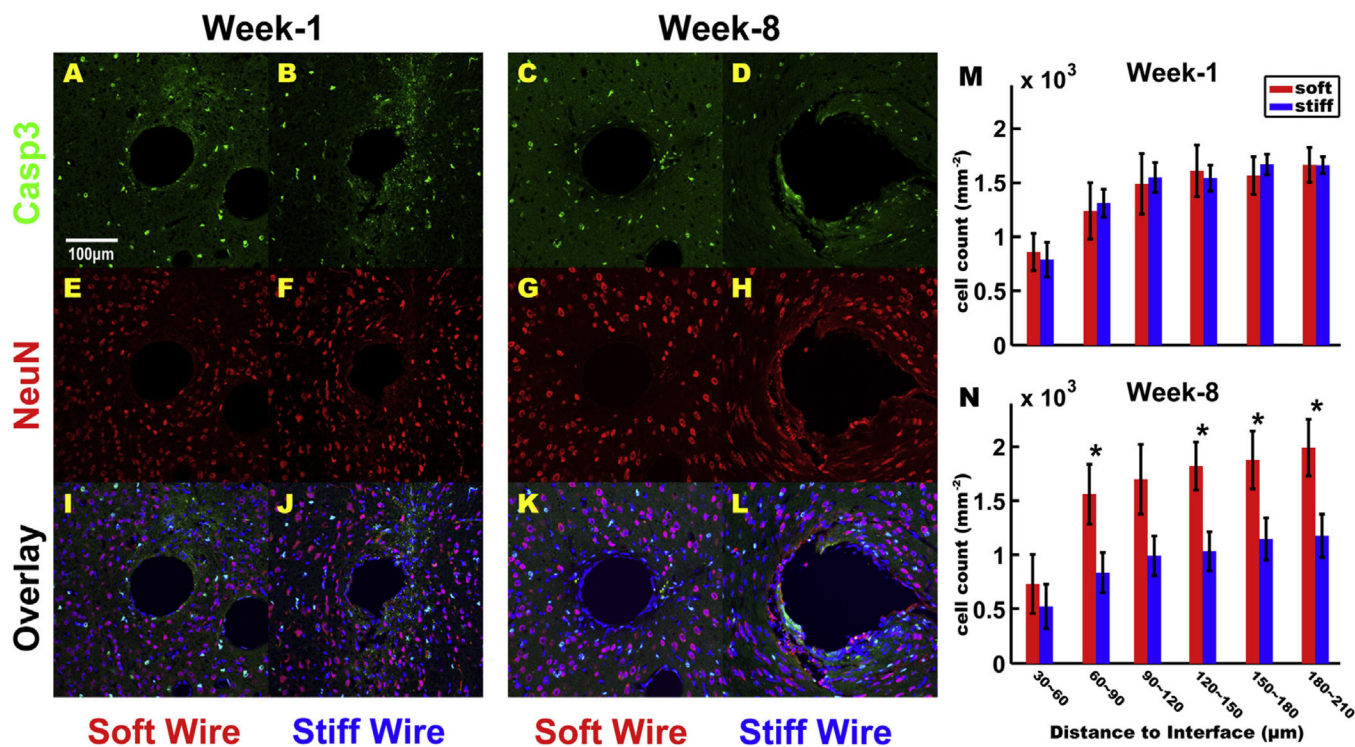
Fig. 3.

Apoptotic cell death around soft and stiff implant. Cleaved Caspase 3 (Casp3) indicates apoptotic cell death and NeuN indicates neurons. Very little co-localization of Casp3 and NeuN was observed in any group. I-L are the overlay of these images with Hoechst. Scale bar = 100 μm. M and N are cell density counts per mm^2 at week-1(soft N = 14, stiff N = 13) and week-8(soft N = 10, stiff N = 11), respectively; cell counts were calculated by automated analysis of NeuN staining and the result was binned 30 μm from the electrode-tissue interface until 210 μm away, with 30 μm bin size. Bins start 30 μm from the interface because cell count within 30 μm of the interface were too low, yielding inaccurate results.
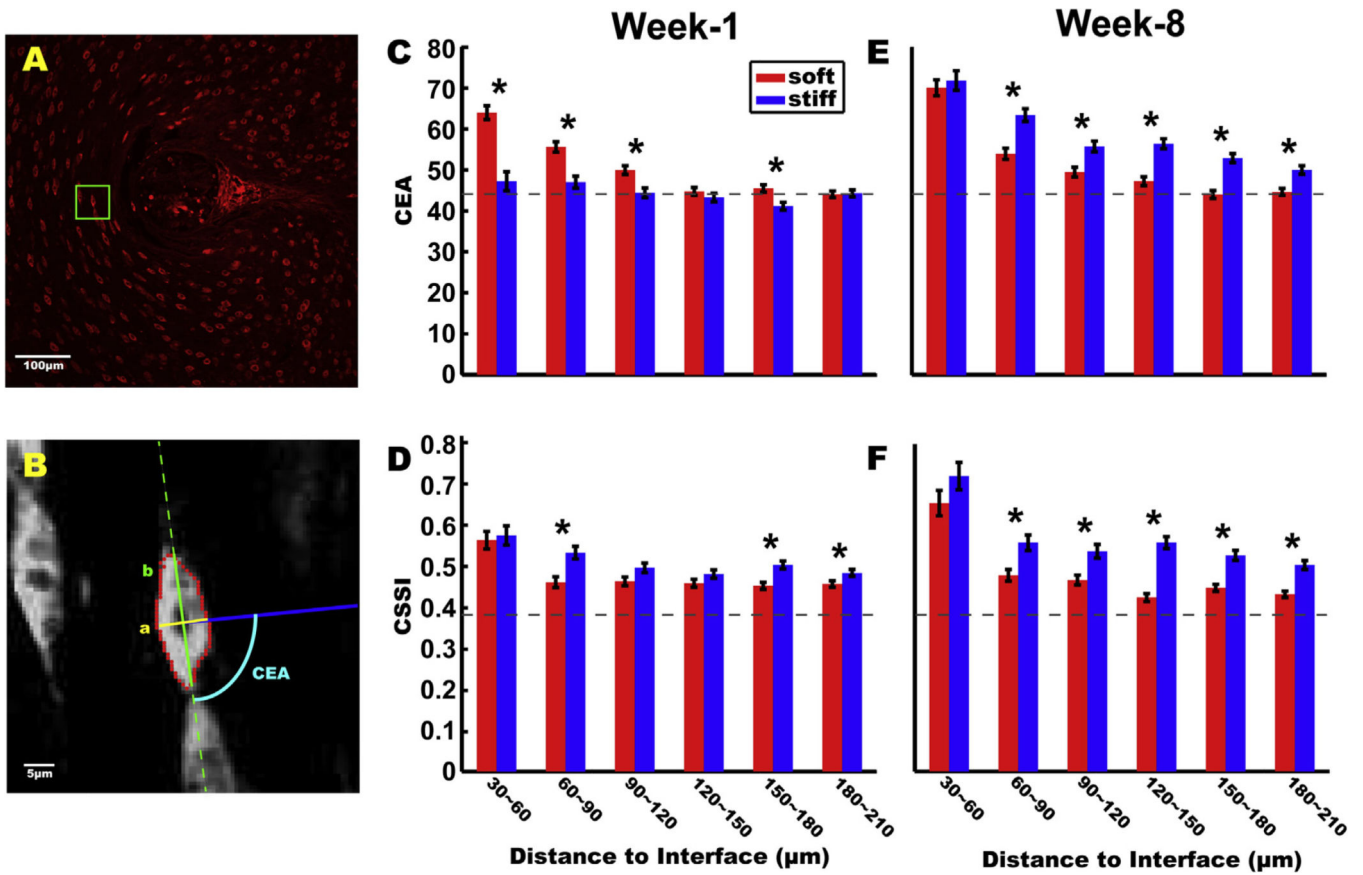
Fig. 4.
Neuronal cell deformation around soft and stiff implants. A. Example image of NeuN staining for week-8 around a stiff implant. Neurons on the left side of the image show significant distortion possibly caused by the micro-motion related strain from the implant. Scale bar = 100 μm. B. Illustration of CEA and CSSI definitions exemplified by a post-processed cell image. Automatical segmentation yielded the red dots as the pixel boundary of the cell. The dashed green line is the long axis direction, the solid green line is the length of the long axis b, the solid yellow line is the length of the short axis a, and the solid blue line is the connection between the center of the cell and the center of the implanted wire. The cyan arc depicts the definition of CEA as the angle between the dashed green line and the solid blue line. Scale bar = 5 μm. C and E are CEA comparisons between soft and stiff wires at week-1 and week-8, respectively. D and F are CSSI comparisons between soft and stiff wires at week-1 and week-8, respectively. The dashed gray line in each image represents the mean of the CEA or CSSI analysis result from control images in non implanted cortical tissue sections. All results are binned 30 μm from the electrode-tissue interface until 210 μm away, with 30 μm bin size.
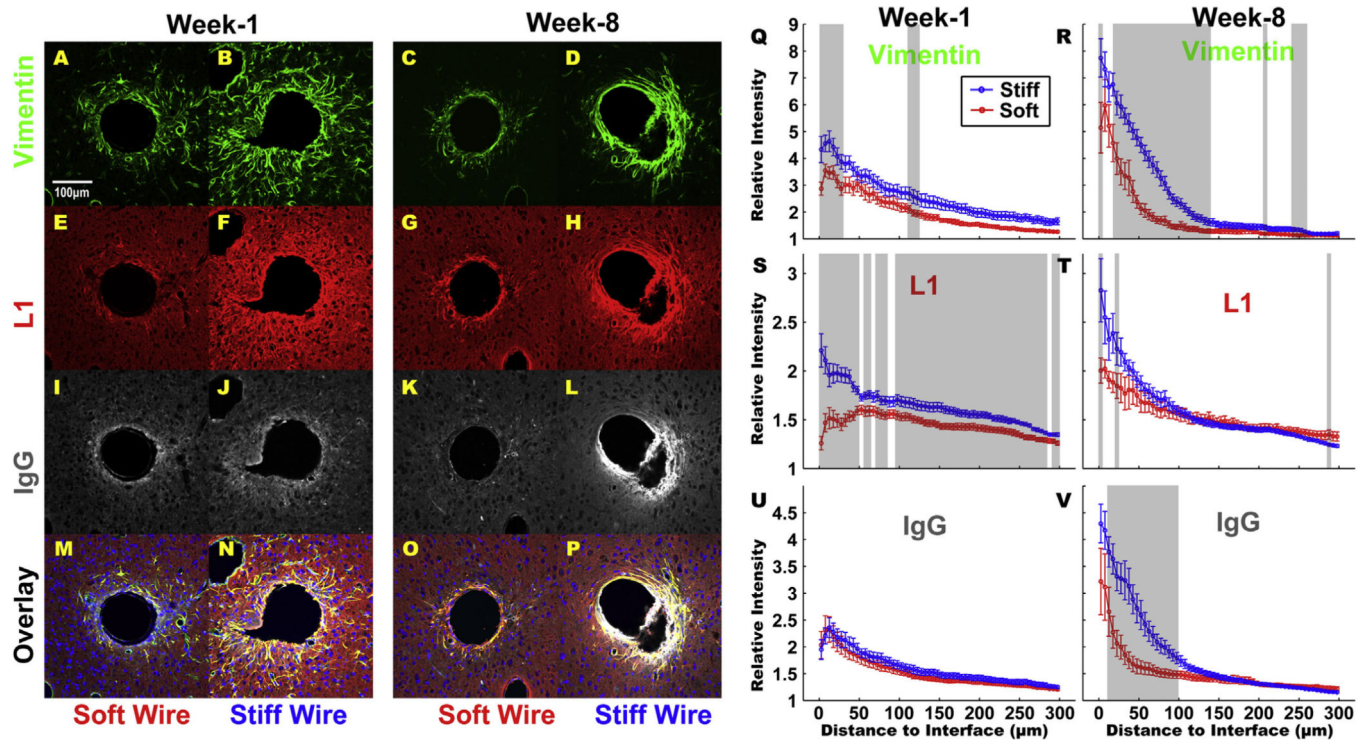
Fig. 5.

Chronic BBB leakage and potential neural regeneration around implants. Vimentin (green) clearly aggregates around both implant types although the stiff wires cause a broad range increase of vimentin expression far from the implant as well. L1 (red) is associated with tissue response as well as possible developing oligodendrocytes for axon repair. Very strong L1 activity is observed around stiff implants at both time points. IgG (gray) indicates BBB leakage. IgG intensity around the stiff implants was very similar to that around soft wires at week 1 but became much stronger at week 8, indicating a significant chronic leakage of the BBB caused by the stiff implant. Scale bar = 100 μm. Q and R are normalized intensity values for Vimentin at week-1(soft $N = 9$, stiff $N = 8$) and week-8(soft $N = 8$, stiff $N = 10$), respectively; S and T are normalized intensity values for L1(week-1 soft $N = 10$, stiff $N = 8$, week-8 soft $N = 9$, stiff $N = 10$); U and V are normalized intensity values for IgG(week-1 soft $N = 10$, stiff $N = 9$, week-8 soft $N = 10$, stiff $N = 11$). Intensities are calculated 0 μm from the electrode-tissue interface until 300 μm away, with 5 μm bin size. Q and S demonstrate a broad range increase of Vimentin and L1 around stiff implants at week-1. R, T and V all indicate that a significant portion of the chronic tissue response was caused by the mechanical properties of the stiff implant. (For interpretation of the references to colour in this figure legend, the reader is referred to the web version of this article.)
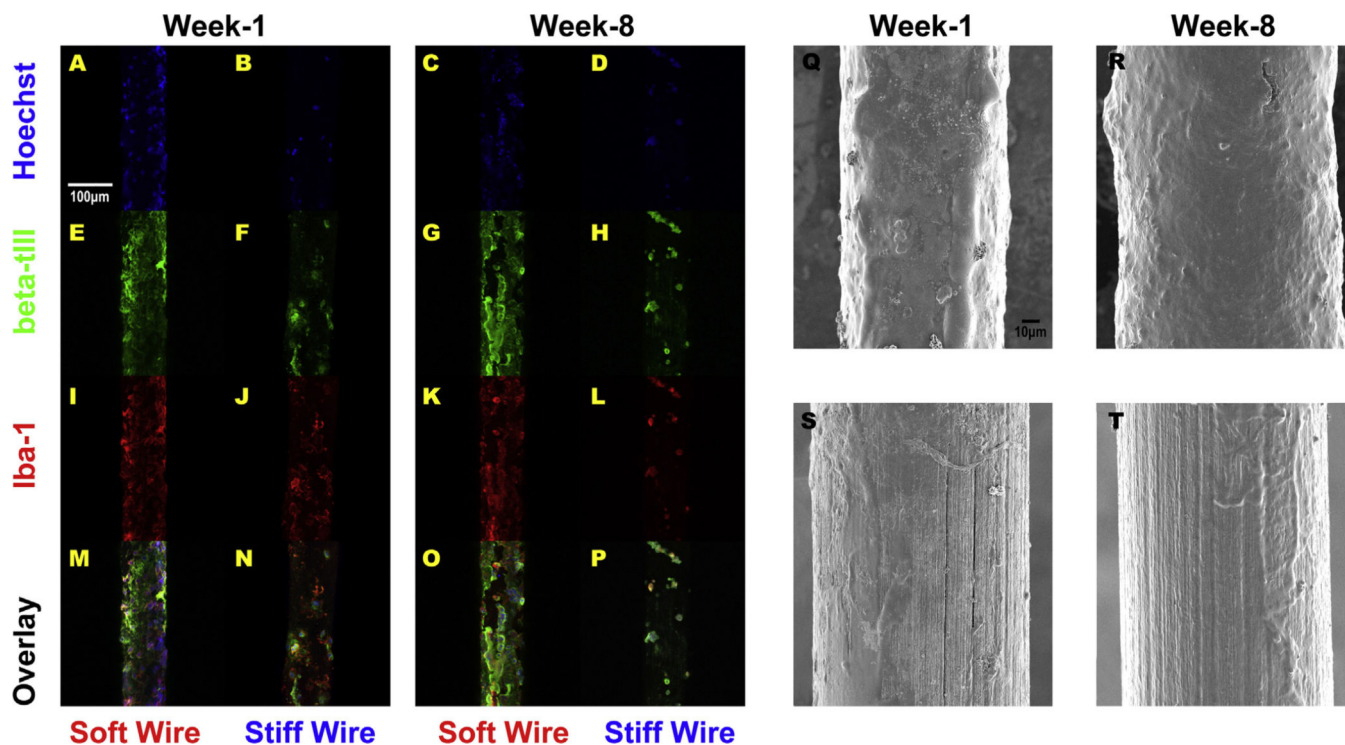
Fig. 6.
Cell adhesion and surface morphology of explanted soft and stiff implants. Hochest (blue), beta-III tubulin (green) and Iba-1 (red) exhibit uniform and confluent coverage on soft wires at week-1 and week-8 with dominant beta-III tubulin expression. In comparison, the cells on stiff wires are scattered with Iba-1 domanance especially at week-1, indicating the stiff wires have poor integration with tissue and that microglia cells are preferentially attracted to this surface. Each image is the reconstruction of 11 z-stack confocal microscope images. Scale bar = 100 μm. Q-T illustrate the wire morphology under SEM imaging. The insulation layer on the stiff wire is visible at both week-1 and week-8. At week-8, the soft wire not only attracted a layer of cells, but also exhibited a bulky tissue shell consisting mostly of neural cells according to beta-III tubulin intensity in G and overlay image O. SEM scale bar = 5 μm. (For interpretation of the references to colour in this figure legend, the reader is referred to the web version of this article.)
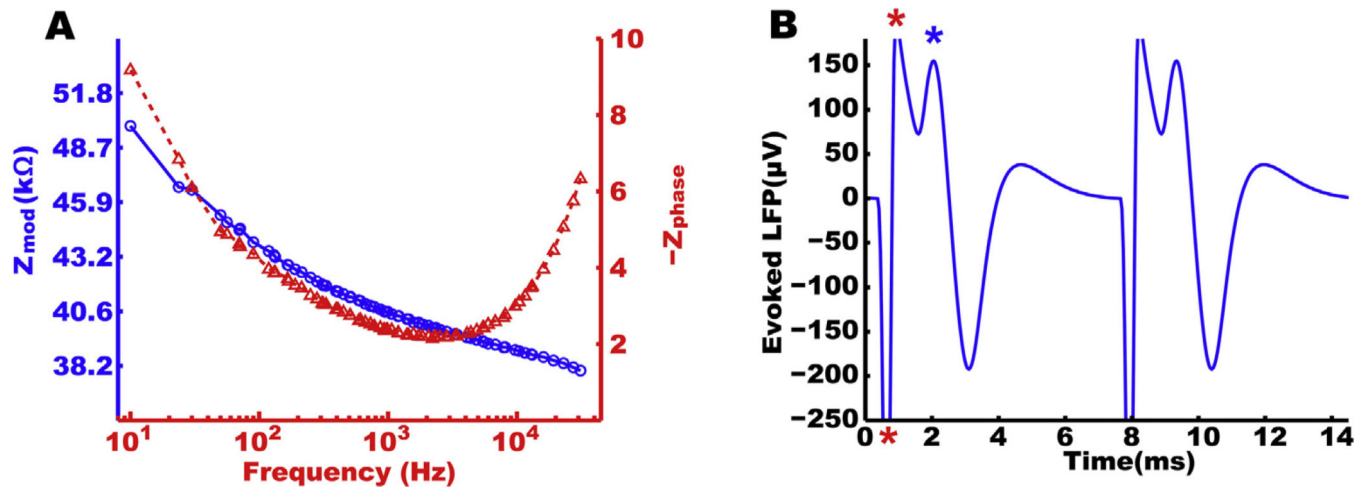
Fig. 7.
Impedance and DBS performance of the elastomer electrode. A. Impedance spectrum of the elastomer electrode for neural stimulation. A thin layer of gold is sputtered on the side of the conductive elastomer core to provide better conductivity. Very low impedance is recorded on the polymer electrode to prove the neural stimulation capability. B. STN DBS with the soft wire evoked a strong LFP in the ipsilateral motor cortex recorded by a ground screw EEG. Stars denote the electrical stimulation artifacts.

Table 1

Antibodies used for histological characterization.

Antibody	Specificity
NF200	Mature axons
Iba1	Microglia/macrophages
GFAP	Astrocytes
Caspase-3	Cleaved (activated) caspase-3
NeuN	Neuronal nuclei
Vimentin	Immature and reactive astrocytes, microglia, endothelial cells, fibroblasts
L1	Neural cell adhesion molecule
IgG	IgG protein, especially from BBB leakage
Beta-III Tubulin	Neuron microtubules